

*Research Article*

# **Flood risk assessment from high tide based on principal component analysis (PCA) of Sentinel-1 satellite images sequence for Ho Chi Minh City**

**Doan Ha Phong<sup>1\*</sup>**

<sup>1</sup> Viet Nam institute of Meteorology, Hydrology & Climate Change; dhphong@gmail.com

\*Correspondence: dhphong@gmail.com; Tel.: +84–913212325

Received: 8 June 2023; Accepted: 24 July 2023; Published: 25 September 2023

**Abstract:** Using Sentinel-1 image series with 10m resolution from the past to present by Principal Component Analysis (PCA) method for Ho Chi Minh City area, helping to assess flood risk due to canal leveling, slitting in some complicated times, narrows the space for water regulation. In addition, Climate change causes sea level rise, thereby increasing the existing water level along with that in large rivers and also causing storm surge, which coincides with the time of flood discharge at Dau Tieng and Tri An reservoirs. The situation of groundwater exploitation, subsidence of the existing ground is continuous and increasing. With the accumulated settlement estimated to date about 100 cm, the current settlement rate is about 2-5 cm per year. Particularly in concentrated areas such as commercial works, the subsidence rate is about 7-8 cm per year. The rate of land subsidence is about twice as high as sea level rise. Therefore, Ho Chi Minh City is one of the cities affected by flooding due to high tide, especially in the current climate change conditions. According to the statistics of flood-prone areas due to high tides from 2014 to 2022, Can Gio district has the highest risk of flooding, with a flooded area of up to 3.713.236 hectares. The districts with an extremely high risk of flooding after Can Gio district are Cu Chi district, Binh Chanh district, and Nha Be district, with 1,764,564 ha, and 1,296,246 ha, and 1,012,550 hectares.

**Keywords:** Satellite image; Sentinel-1; Flood risk; Principal Component Analysis; High Tides.

---

## **1. Introduction**

Statistical and near-real-time information about flooded areas is necessary for several public services, e.g., emergency, rescue, rehabilitation, spatial planning, habitat monitoring, and adapting to climate change. Remote Sensing satellites can provide operational and timely data as well as spatial information on flooded areas covered by water. Two types of satellite imagery are available to monitor flood dynamics on the surface: optical aperture radar (OAR) and data radar (SAR). Optical remote sensing can only be applied in cloudless situations. However, flooding often occurs during periods of prolonged rain and frequent cloud cover. Therefore, SAR systems are often the preferred tool for monitoring floods from space. The flat, water surface is characterized by low SAR backscatter, and the difference in backscatter reflectance often enables flood mapping [1]. Using a combination of different SAR image data such as COSMO-SkyMed and Sentinel-1, or combined with Flood Research Optical images such as MODIS and terraSAR-X [2–5], monitor inundation changes thanks to the advantage of multi-temporal images and through surface cover indices [6–10], through the dynamic identification of the water-marked area [11], using the urban area marker [11–15], and using backscatter signals from SAR images to detect and mark the rapid evolution of flooded areas, especially flooding caused by high tides [16–18]. Based on the summary of A

local thresholding approach to flood water delineation [8, 18], the most applied method to map floods from a single image is the threshold histogram, which can be used in conjunction with other image processing methods. different photos. Time change detection techniques [19–20] and associative analysis [21] have also been used to map open water. However, time-varying detection methods require two images and may therefore be limited by the temporal coverage of the satellite images. To improve the accuracy of flood maps, the advantages of ancillary data, such as the HAND index (elevation above the nearest drainage) are derived from the DEM (digital elevation model) and the DIST index (distance from drainage system) are derived from the watershed as well as the land use map, which has been demonstrated in several studies [17, 18, 20, 22]. Most of the proposed methods for flood mapping are semi-automatic. A fully automated method integrating thresholding separation and fuzzy logic classifiers has been proposed and applied by the author [18] for TerraSAR-X processing and by the author [23] to process Sentinel-1 (S1).

Recent research by the authors [24–25] summarized the methods of mapping flooding under the forest canopy. Research by the author [24] showed that the most applied method to detect submerged areas under vegetation is to identify increased backscatter values compared with other objects. The penetration depth of SAR signals into vegetation is higher for longer wavelengths, so the use of L-band has been recommended [26, 27–28]. However, several studies [20, 29–30] have demonstrated the ability of C-band and X-band data to identify submerged vegetation, especially in the case of sparse forest and leafless forests. Co-polarization signals (HH or VV) are preferred over cross-polarized signals for mapping water under vegetation. Studies have shown that using HH polarization leads to more accurate results than VV polarization [31–32]. Furthermore, the use of polarization analysis and/or an interferometric SAR combination has been used to map flooding under vegetation [33]. However, the availability of full polarization data is often limited in terms of spatial extent and temporal coverage.

Sentinel-1 images have modes (i) single polarized VV (Vertical-Vertical) or HH (Horizontal) and (ii) double polarized VH (Vertical-horizontal) or HV (Horizontal-Vertical). investigated the effects of single VV and double VH polarization for flood monitoring in the Ebro River Basin, Spain, using Sentinel-1 images [34]. A combination of Sentinel1 and Landsat images for inundation area identification and flood impact monitoring for the Houston, Central Greece, and East Coast of Madagascar regions of the United States [35]. The results from the above studies all confirmed that the VV polarization for inundation monitoring results is quite suitable for building flood maps using Sentinel-1 images. The above examples demonstrate that VV polarization can be used to determine the water surface area with rapid variation and is well suited to the observation of high tides.

In the past, the creation of flood maps often took a lot of time and money using SNAP software. The recent introduction of the Google Earth Engine (GEE) cloud platform has increased the convenience of research [36–37], providing powerful computing resources for free. GEE has been widely used in large-scale and long-term flood dynamics monitoring missions [38–40]. Another advantage of this platform is that it provides multiple datasets, facilitates data collection, and allows researchers to use different datasets for collaborative analysis to improve data collection and algorithmic accuracy [41–42].

Simultaneous operation of 2 satellites, Sentinel 1A and Sentinel 1B, allows to shorten the time of image acquisition at a location on the earth's surface to 6 days (compared to 12 days if only 1 satellite is used). The sensor on the Sentinel-1 satellite acquires a composite open aperture radar image, channel C.

## **2. Methodology**

### *2.1. Description of study site*

**Topographic:** Overall, HCMC has a relatively flat and low terrain with several West-North and east-northeast slopes, the height of the ground tends to decrease gradually from the North-West to the South and Southeast.

The area is largely distributed into the districts: Cu Chi, Hoc Mon, north of Thu Duc City, district 9, north of Binh Chanh district. Heights from 4-10 m account for about 19% of the total area; areas with heights above 10 m account for 11% of total area.

The lowland is distributed in the inner city, the land in Hoc Mon district, Thu Duc city, and the southern part of Binh Chanh district is located along the Saigon River; the elevation of this area varies from 2-4 m, accounting for about 15% of the whole area of Ho Chi Minh City. The low-lying valley comprises a steep slope running from the south of Cu Chi district, with an altitude of 0-2 m, and accounts for approximately 55% of Ho Chi Minh City's land area.

**Hydrology:** Located in the basin of the Dong Nai-Saigon river system, the hydro-hydraulic mechanism of the canals and rivers is not only influenced by the topography of Ho Chi Minh City (mostly less than 2 m), the semi-diurnal regime of the East Sea, but also by the exploitation of terraced lakes upstream now and in the future, such as Tri An, Dau Tieng, Thac Mo lakes.

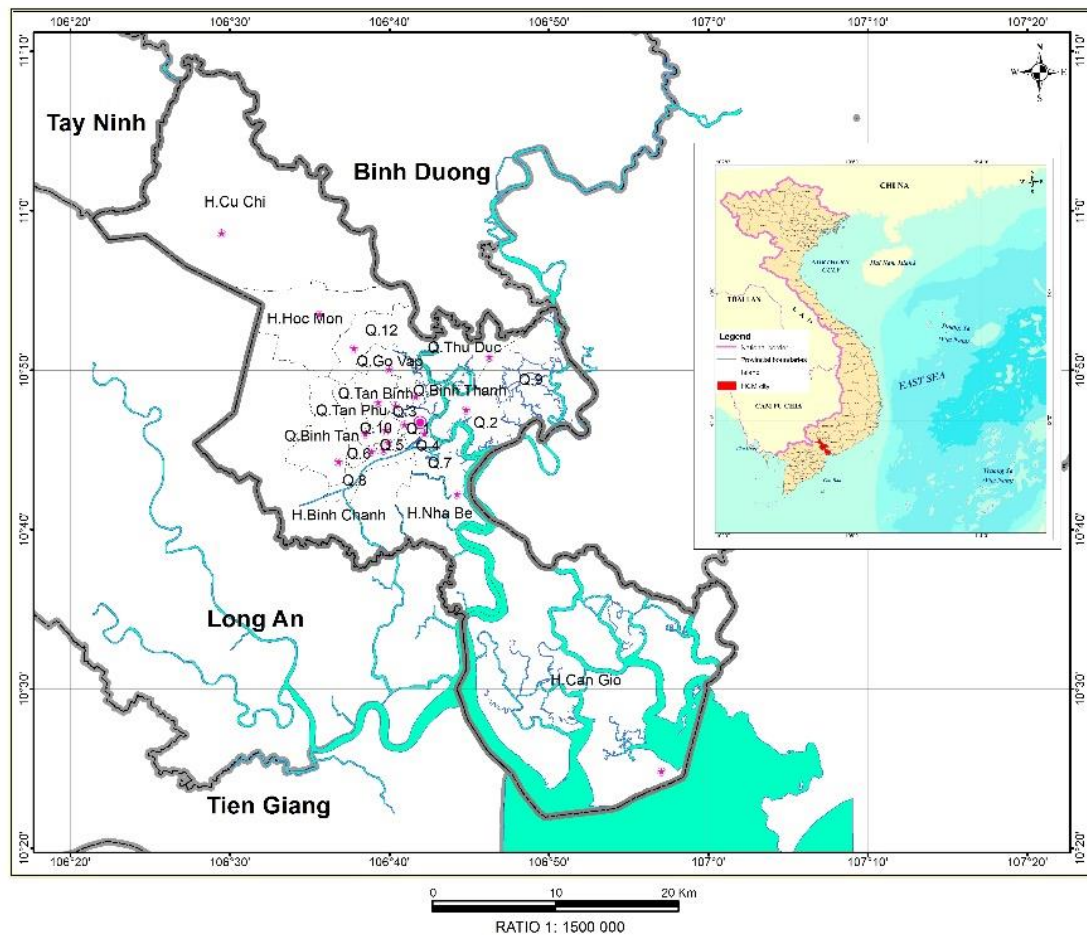


**Figure 1.** Map of Ho Chi Minh City in Vietnam.

The river system has a total length of 7,955 km; the total water surface area accounts for 16%; the average flow density is 3.80 km<sup>2</sup>... Thus, the valley low terrain has an altitude of less than 2 m and the water surface represents 61% of the natural area, is located in the river gate area with many large regulatory works at the top of the source so the risk of flooding occurs in a wide area.

**Rainfall:** Total average rainfall in Ho Chi Minh city is quite high from 1800 mm to 2700 mm, concentrating on July from May to November accounting for up to 90% of rainfall.

Hydrological regimes: Since there are two main seasons of the rainy season and the dry season, the flow mode in the two systems of the Saigon River and the Dong Nai River also forms two respective flow modes. At the same time, due to the impact of the East Sea, the rivers of the inner city of Ho Chi Minh city are affected by the tide strongly and throughout the year. Here is the semi-diurnal tides regime shown through the fluctuations:

The moon fluctuates: two times of high tide and two times of low tide; the time of high tide is 50 minutes back compared to the previous day. Seasonal developments: There are two high tides in a month (from the 27<sup>th</sup> day of the previous month to the 5<sup>th</sup> of the following month and from the 13<sup>th</sup> to the 18<sup>th</sup> of the solar calendar). Seasonal fluctuation: Spring tides (days 11, 12, and 1 of the solar calendar): this period is maintained by the flow of the rainy season in the inner city, so the high tide period usually lasts from September to January of the solar calendar.

Subsidence: By synthesizing the results of high-speed measurements in the Ho Chi Minh city region and the Mekong River Delta in 2017, 2018 of the Ministry of Natural Resources and Environments showed the land in Ho Chi Minh city and the provinces of the Cuu Long river valley is falling down the main causes are:

- The group of natural causes such as the displacement of the plates, the soil processes attempting to end up dehydrating and the natural contraction of the layer of an early Holoxen sediment.
- The group of human-influenced causes such as underground water mining, urbanization increases the load on weak soil, vibration due to traffic activities.

Based on the Subsidence partition shows that Ho Chi Minh city is falling at a high rate of more than 10 cm in 10 years in the district of Binh Chanh, southern of Binh Tan district, district 8, district 7, east district 12, western district of Thu Duc, northern districts of Nha Be with a total area of 239 km<sup>2</sup>. Especially where it dropped to 73 cm/10 years, from 2005-2015.

## 2.2. Method

Principal Component Analysis (PCA) operator, this operator generates the principal component images from a stack of co-registered detected images.

The PCA consists of a remapping of the information of the input co-registered images into a new set of images. The output images are scaled to prevent negative pixel values. The PCA operator consists of the following major steps:

Average the pixels across the input images to compute a mean image. Optionally subtract the computed mean image from each input image.

Subtract the mean value of each input image (or image from Average step) from itself to produce zero-mean images.

Compute covariance matrix from the zero-mean images given in Subtract step. Perform eigenvalue decomposition of the covariance matrix.

Compute PCA images by multiplying the eigenvector matrix by the zero-mean images given in Subtract step. Here the user can select the eigenvectors instead of using all vectors. The selection is done with a user input threshold, which is in

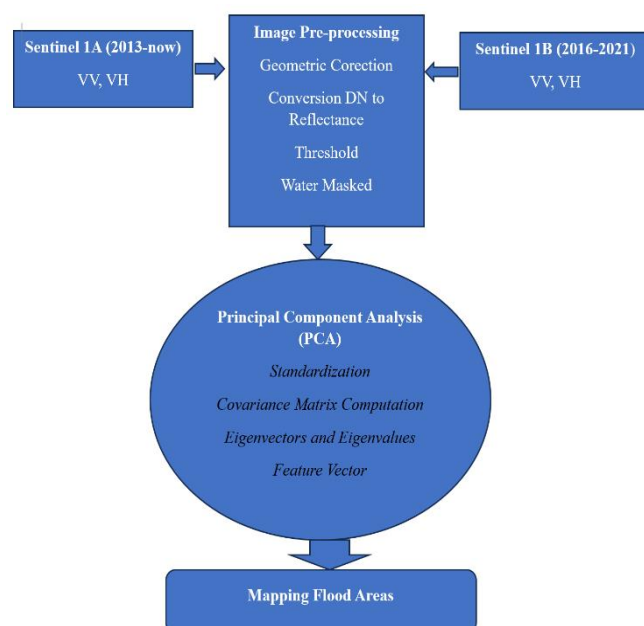


**Figure 2.** Flowchart of study structure.

percentage, on the eigenvalues. For example, in the case of three input images,  $a_1$ ,  $a_2$  and  $a_3$  (where  $a_1 \gg a_2 \gg a_3$ ) are the eigenvalues, if the threshold is 80% and  $(a_1+a_2) \gg 80\%$ , then  $a_3$  will not use in computing the PCA images. Only two PCA images will be produced.

The flowchart of study structure on principal component analysis (PCA) of Sentinel-1 satellite images sequence for Ho Chi Minh City (Figure 2).

The following parameters are calculated from the Sentinel 1 image data series for the period 2014-2022 in the Ho Chi Minh City area:

Source range: The VV polarization band is selected to perform PCA for the marking of flood-prone areas and other causes of flooding.

Eccentricity threshold: Threshold used in eigenvalue selection to produce the final PCA image. These are the values determined from the series of VV polarization values for the period 2014-2022, suitable for each year.

Show eigenvalues: Defines eigenvalues to be displayed automatically in areas flooded by high tides.

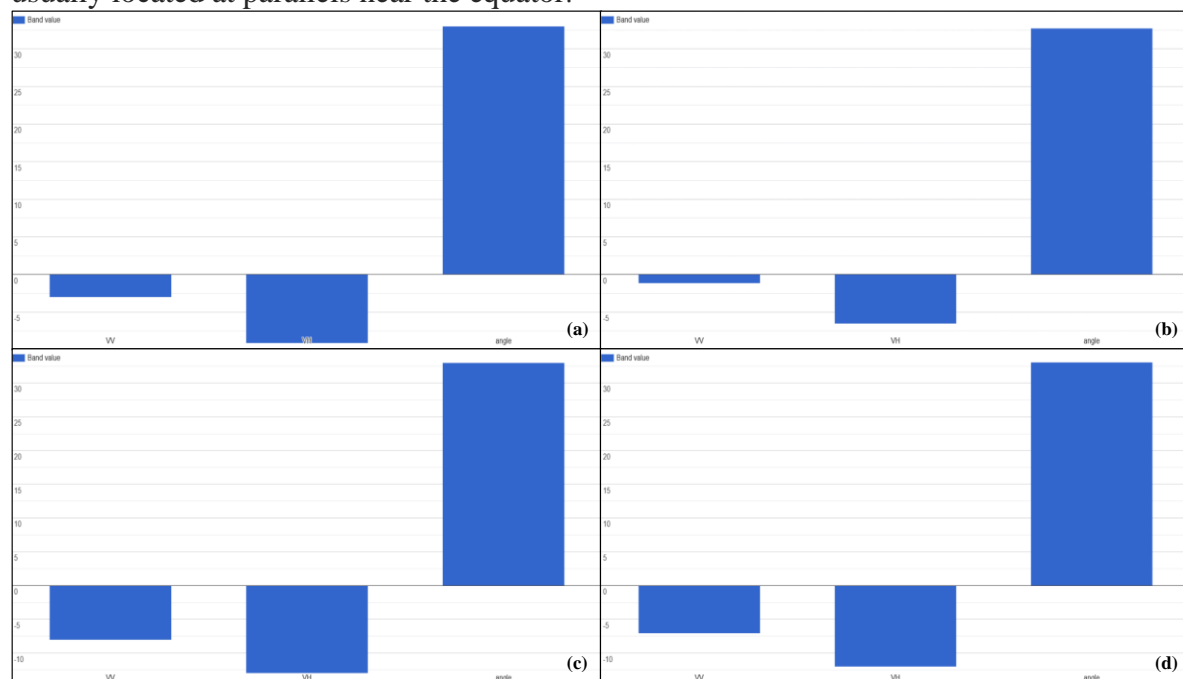
Subtracting the average image: The average image of the input images for the period 2014-2022 (September-January next year) is subtracted from each input image before applying PCA.

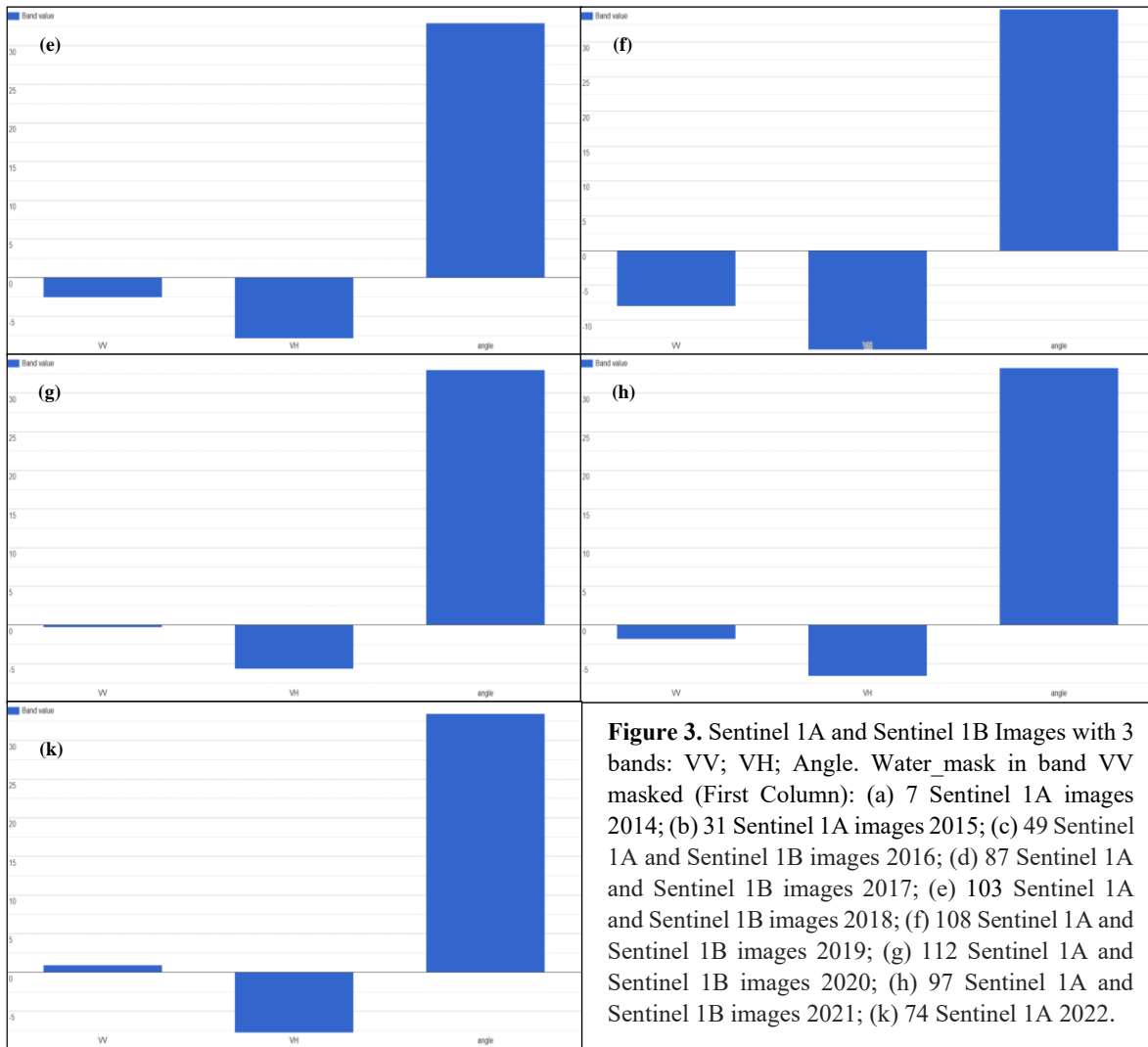
### 2.3. Data

Sentinel-1A was launched on 3 April 2014, and Sentinel-1B on 25 April 2016. They orbit  $180^\circ$  apart, together imaging the Earth every six days.

The two-satellite SENTINEL-1A and SENTINEL-1B constellation offers a 6-day exact repeat cycle. The constellation will have a repeat frequency (ascending/descending) of 3 days at the equator is expected to provide coverage over Ho Chi Minh city and main shipping routes in 1-3 days, regardless of weather conditions. Radar data will be delivered to Copernicus services within an hour of acquisition.

In December 2021, an anomaly in the power supply of Sentinel-1B caused the SAR sensor to stop working. Attempts to restore power to the sensor failed, and the mission officially ended on August 3, 2022. The highest tides of the year usually appear in October and November of the lunar calendar. The tidal regime in Ho Chi Minh City has a semi-diurnal tidal regime, with two high and low tides per day. The area affected by this type of tide is usually located at parallels near the equator.





The backscatter coefficients under VV polarization for the water area are lower than those under VH polarization (around 0–7 dB) (Figure 3a-3k).

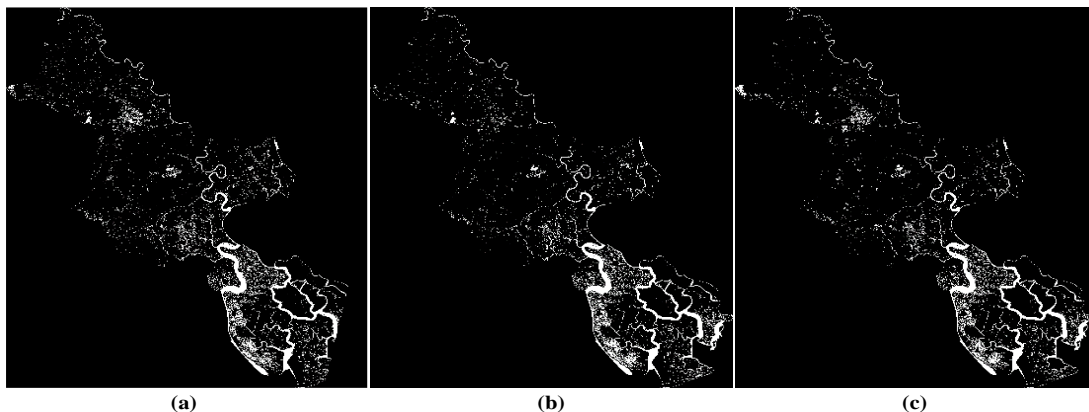
### 3. Results

#### 3.1. Standardization

The aim of this step is to standardize the range of flood variables due to by continuous tides for years 2014 to 2022 to contributes equally to the analysis:

$$z = \frac{\text{value} - \text{mean}}{\text{standard deviation}} \tag{1}$$

Once the standardization is done, all the variables will be transformed to the same scale, a flood tides variable that 0 and 1.



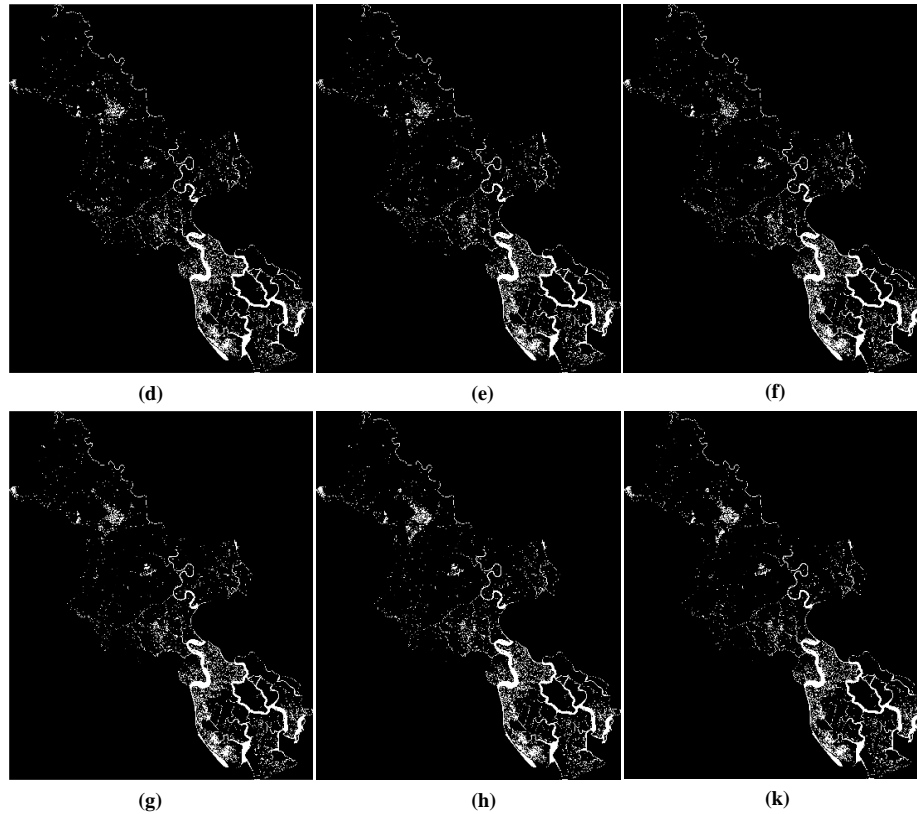


**Figure 4.** High tide based on principal component analysis (PCA) of Sentinel-1 satellite images sequence for Ho Chi Minh City. The image shows the distribution of flooding caused by high tide in Ho Chi Minh City from September to January next year in the period 2014–2022: (a) Flood tides 2014 (Component 1); (b) Flood tides 2015 (Component 2); (c) Flood tides 2016 (Component 3); (d) Flood tides 2017 (Component 4); (e) Flood tides 2018 (Component 5); (f) Flood tides 2019 (Component 6); (g) Flood tides 2020 (Component 7); (h) Flood tides 2021 (Component 8); (k) Flood tides 2022 (Component 9).

The Can Gio area is the area most affected by high tide from 2014 to 2022 from Sentinel-1A and Sentinel-1B. In addition, the regional city centers of Cu Chi district, Binh Chanh district, and Nha Be district are affected (Figure 4a-4k).

### 3.2. Covariance matrix computation

The variables of the input data set vary from the mean with respect to each other, to see if there is any relationship between them. Because sometimes, variables are highly correlated in such a way that they contain redundant information. To identify these correlations, we compute the covariance matrix from 0.3588 to 0.3746 will be selected. The covariance matrix is a  $9 \times 9$  symmetric matrix (where 9 is the number of dimensions) that has as entries the covariances associated with all possible pairs of the initial variables (Table 1).

**Table 1.** Covariance matrix for 9-dimensional flood tides data year 2014 to 2022.

	1	2	3	4	5	6	7	8	9
1	<b>0.0370</b>	0.0288	0.0284	0.0280	0.0272	0.0278	0.0271	0.0270	0.0262
2	0.0288	<b>0.0359</b>	0.0310	0.0303	0.0296	0.0301	0.0293	0.0291	0.0282
3	0.0284	0.0310	<b>0.0358</b>	0.0317	0.0306	0.0308	0.0302	0.0302	0.0292
4	0.0280	0.0303	0.0317	<b>0.0363</b>	0.0318	0.0319	0.0311	0.0309	0.0301
5	0.0272	0.0296	0.0306	0.0318	<b>0.0353</b>	0.0324	0.0314	0.0312	0.0302
6	0.0278	0.0301	0.0308	0.0319	0.0324	<b>0.0374</b>	0.0329	0.0325	0.0316
7	0.0271	0.0293	0.0302	0.0311	0.0314	0.0329	<b>0.0362</b>	0.0330	0.031
8	0.0270	0.0291	0.0302	0.0309	0.0312	0.0325	0.0330	<b>0.0370</b>	0.0328

	<b>1</b>	<b>2</b>	<b>3</b>	<b>4</b>	<b>5</b>	<b>6</b>	<b>7</b>	<b>8</b>	<b>9</b>
<b>9</b>	0.0262	0.0282	0.0292	0.0301	0.0302	0.0313	0.0313	0.0328	<b>0.0359</b>

*3.3. Compute the eigenvectors and eigenvalues of the covariance matrix to identify the principal components*

Eigenvectors and eigenvalues are the linear algebra concepts that we need to compute from the covariance matrix to determine the principal components of the flood tides data. Principal components are new variables that are constructed as mixtures of the initial variables. These combinations are done in such a way that the new variables (i.e., principal components) are uncorrelated and most of the information within the initial variables is squeezed or compressed into the first components. So, the idea is 9-dimensional data gives you 9 principal components, PCA tries to put maximum possible information in the first component, then maximum remaining information in the second and so on Table 2.

**Table 2.** Eigenvectors of flood tides data year 2014 to 2022.

1	0.3079	0.7306	0.5768	-0.1828	-0.0699	-0.0020	-0.0003	-0.0096	-0.0115
2	0.3265	0.3343	-0.3588	0.5572	0.5064	0.2598	-0.1334	-0.0143	0.0154
3	0.3335	0.1791	-0.4010	0.1740	-0.4008	-0.6055	0.3703	-0.0233	-0.0196
4	0.3386	0.0219	-0.3455	-0.2906	-0.4377	0.3101	-0.4929	0.3839	0.0524
5	0.3358	-0.0955	-0.1930	-0.3903	0.0136	0.3148	0.2004	-0.7386	-0.0354
6	0.3450	-0.1788	-0.0168	-0.4138	0.4905	-0.0814	0.3916	0.4743	0.2271
7	0.3395	-0.2628	0.0144	-0.0633	0.2367	-0.3928	-0.4154	-0.0610	-0.6356
8	0.3406	-0.3214	0.3027	0.2362	-0.0554	-0.1992	-0.2975	-0.2076	0.6772
9	0.3308	-0.3289	0.3289	0.3945	-0.2938	0.4120	0.3838	0.18519	-0.2844

*3.4. Feature vector*

As we saw in the previous step, computing the eigenvectors and ordering them by their eigenvalues in descending order (0.27831-0.00332), allow us to find the principal components in order of significance. In this step, what we do to choose whether to keep all these components or discard those of lesser significance (of low eigenvalues), and form with the remaining ones a matrix of vectors that we call feature vectors. This makes it the first step towards dimensionality reduction, because if we choose to keep only 7 eigenvectors (components) out of 9:

**Table 3.** Percent and accumulative eigenvalues.

<b>Component</b>	<b>Eigen value</b>	<b>Percent of eigen values</b>	<b>Accumulative of eigen values</b>
2014	0.2783	85.0812	85.0812
2015	0.0141	4.4332	89.4137
2016	0.0085	2.5978	92.0115
2017	0.0059	1.8324	93.8439
2018	0.0052	1.5943	95.4382
2019	0.0042	1.2951	96.7334
2020	0.0037	1.1560	97.8894
2021	0.0035	1.0968	98.9862
2022	0.0033	1.0138	100.000

**Table 4.** Mean vector.

	<b>Mean vector</b>
2014	0.0384
2015	0.0373
2016	<b>0.0372</b>
2017	0.0377
2018	<b>0.0366</b>

Mean vector	
2019	0.0389
2020	0.0376
2021	0.0385
2022	0.0373

This makes it the first step towards dimensionality reduction, because if we choose to keep only 9 eigenvectors (components) out of 9, the final data set will have only 7 dimensions. 2016 and 2018 are the years with outstanding average values of high tide with values 0.0372 and 0.0366.

### 3.5. Recast the data along the principal components axes

In this step, which is the last one, the aim is to use the feature vector formed using the eigenvectors of the covariance matrix, to reorient the data from the original axes to the ones represented by the principal components (hence the name Principal Components Analysis). This can be done by multiplying the transpose of the original data set by the transpose of the feature vector.

$$\text{Final Data Set} = \text{Feature Vector}^T * \text{Standardized Original Data Set}^T \quad (2)$$

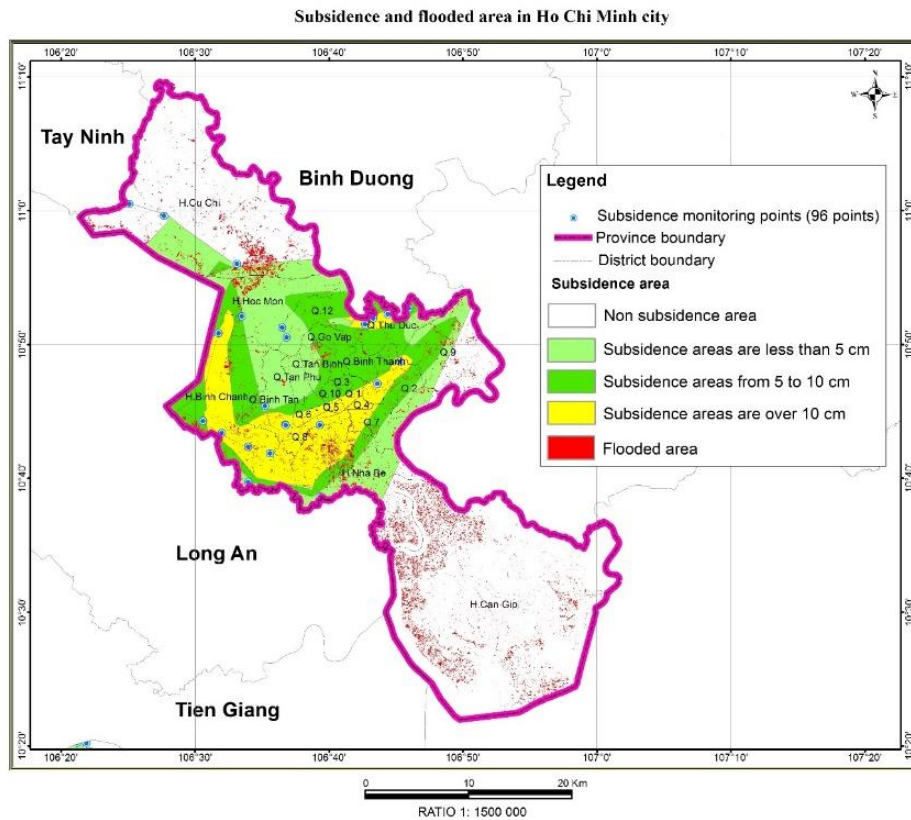


Figure 4. Flood risk assessment from high tide based on Sentinel-1 satellite for Ho Chi Minh City.

Table 5. Basic vector.

	C1	C2	C3	C4	C5	C6	C7	C8	C9
2014	0.3079	0.3265	0.3335	0.3386	0.3358	0.3450	0.3395	0.3406	0.3308
2015	<b>0.7306</b>	0.3343	0.1791	0.0219	-0.0955	-0.1788	-0.2628	-0.3214	-0.3289
2016	<b>0.5768</b>	-0.3588	-0.4010	-0.3455	-0.1930	-0.0168	0.1448	0.3027	0.3285
2017	-0.1828	<b>0.5572</b>	0.1740	-0.2906	-0.3930	-0.4138	-0.0633	0.2362	0.3945
2018	-0.0699	<b>0.5064</b>	-0.4008	-0.4377	0.01361	0.4905	0.2367	-0.0554	-0.2938
2019	0.0019	-0.2598	<b>0.6055</b>	-0.3101	-0.3148	0.0814	0.3928	0.1992	-0.4120
2020	<b>3.8316</b>	0.1334	-0.3703	0.4928	-0.2004	-0.3916	0.4154	0.2975	-0.3838
2021	-0.0096	-0.0143	-0.0233	0.3839	<b>-0.7386</b>	0.4743	-0.0610	-0.2076	0.1851
2022	-0.0115	0.0154	-0.0196	0.0524	-0.0354	0.2271	<b>-0.6356</b>	<b>0.6772</b>	-0.2844

The basis vector with the largest variance is the most principal (the one that explains more variance from the dataset). The dot product of each basis vector against the sample. Can be used as a measure for membership in the training sample set. High values correspond to a better fit.

#### 4. Discussion

After 2021, only Sentinel 1A will be in operation, so the number of images collected for tidal research will be limited due to the decrease in the number of images collected. Therefore, the results collected for the period 2014–2022 can be used as a document to help study the distribution for the whole of Ho Chi Minh City visually for the period that is not only affected by high tide but also affected by socio-economic activities as well as affected by climate change.

According to the statistics of flood-prone areas due to high tides from 2014 to 2022, Can Gio district has the highest risk of flooding, with a flooded area of up to 3,713,236 hectares. The districts with a very high risk of flooding after Can Gio district are Cu Chi district, Binh Chanh district, and Nha Be district, with 1,764,564 ha, 1296,246 ha, and 1,012,550 hectares, respectively. Binh Chanh district is located in an area with a subsidence of more than 10 cm. Nha Be district is located in the subsidence area below 5cm and over 10 cm. In addition, other areas such as Hoc Mon district (inundated with 545,739 ha), district 2 (inundated with 673,997 ha), district 9 (inundated with 480,466 ha), Tan Binh district (inundated with 472,860 ha), and district 7 (inundated with 428,667 ha) are also at high risk of flooding due to high tides. Areas of District 2, District 7, District 9, and Tan Binh district are also located in the subsidence area of 5-10 cm. Areas with the lowest risk of flooding are District 3 and District 10, with a flooded area of just over 3,9 hectares. However, District 3 and District 10 are areas located in the subsidence area of 5-10 cm.

**Author Contribution:** Conceptualization: D.H.P.; methodology: D.H.P.; Processing of data: D.H.P.; Construction of maps: D.H.P.; Analysis of results: D.H.P.; writing—original draft preparation: D.H.P.; writing—review and editing: D.H.P.

**Conflicts of Interest:** This manuscript is the research work of the collective author, not published anywhere, not copied from previous studies.

#### Reference

1. Ulaby, F.; Moore, R.; Fung, A. Microwave Remote Sensing. Active and Passive, Artech House: Norwood, MA, USA, 1986, 3, pp. 608.
2. Boni, G.; Ferraris, L.; Pulvirenti, L.; Squicciarino, G.; Pierdicca, N.; Candela, L.; Pisani, A.R.; Zoffoli, S.; Onori, R.; Proietti, C.; et al. A Prototype System for Flood Monitoring Based on Flood Forecast Combined with COSMO-SkyMed and Sentinel-1 Data. *IEEE J. Sel. Top. Appl. Earth Obs. Remote Sens.* **2016**, *9*, 2794–2805.
3. Chen, Y.; Fan, R.; Yang, X.; Wang, J.; Latif, A. Extraction of urban water bodies from high-resolution remote-sensing imagery using deep learning. *Water* **2018**, *10*, 585.
4. Martinis, S.; Twele, A.; Strobl, C.; Kersten, J.; Stein, E. A multi-scale flood monitoring system based on fully automatic MODIS and terraSAR-X processing chains. *Remote Sens.* **2013**, *5*, 5598.
5. Pulvirenti, L.; Pierdicca, N.; Chini, M.; Guerriero, L. An algorithm for operational flood mapping from Synthetic Aperture Radar (SAR) data using fuzzy logic. *Nat. Hazards Earth Syst. Sci.* **2011**, *11*, 529–540.
6. Pulvirenti, L.; Pierdicca, N.; Chini, M.; Guerriero, L. Monitoring flood evolution in vegetated areas using cosmo-skymed data: The tuscany 2009 case study. *IEEE J. Sel. Top. Appl. Earth Obs. Remote Sens.* **2013**, *6*, 1807–1816.

7. Uddin, K.; Matin, M.A.; Meyer, F.J. Operational flood mapping using multi-temporal Sentinel-1 SAR images: A case study from Bangladesh. *Remote Sens.* **2019**, *11*, 1581.
8. Liang, J.; Liu, D. A local thresholding approach to flood water delineation using Sentinel-1 SAR imagery. *ISPRS J. Photogramm. Remote Sens.* **2020**, *159*, 53–62.
9. Schlaffer, S.; Matgen, P.; Hollaus, M.; Wagner, W. Flood detection from multi-temporal SAR data using harmonic analysis and change detection. *Int. J. Appl. Earth Obs. Geoinf.* **2015**, *38*, 15–24.
10. Wendleder, A.; Wessel, B.; Roth, A.; Breunig, M.; Martin, K.; Wagenbrenner, S. TanDEM-X water indication mask: Generation and first evaluation results. *IEEE J. Sel. Top. Appl. Earth Obs. Remote Sens.* **2013**, *6*, 171–179.
11. Chini, M.; Pulvirenti, L.; Pierdicca, N.; Guerriero, L. Multi-temporal segmentation of Cosmo-SkyMed SAR data for flood monitoring. In Proceedings of the 2011 Joint Urban Remote Sensing Event—JURSE 2011, Munich, Germany, 11–13 April 2011.
12. Chini, M.; Hostache, R.; Giustarini, L.; Matgen, P. A hierarchical split-based approach for parametric thresholding of SAR images: Flood inundation as a test case. *IEEE Trans. Geosci. Remote Sens.* **2017**, *55*, 6975–6988.
13. Giustarini, L.; Hostache, R.; Matgen, P.; Schumann, G.J.P.; Bates, P.D.; Mason, D.C. A change detection approach to flood mapping in Urban areas using TerraSAR-X. *IEEE Trans. Geosci. Remote Sens.* **2013**, *51*, 2417–2430.
14. Giustarini, L.; Hostache, R.; Kavetski, D.; Chini, M.; Corato, G.; Schlaffer, S.; Matgen, P. Probabilistic Flood Mapping Using Synthetic Aperture Radar Data. *IEEE Trans. Geosci. Remote Sens.* **2016**, *54*, 6958–6969.
15. Greifeneder, F.; Wagner, W.; Sabel, D.; Naeimi, V. Suitability of SAR imagery for automatic flood mapping in the Lower Mekong Basin. *Int. J. Remote Sens.* **2014**, *35*, 2857–2874.
16. Manjusree, P.; Prasanna Kumar, L.; Bhatt, C.M.; Rao, G.S.; Bhanumurthy, V. Optimization of threshold ranges for rapid flood inundation mapping by evaluating backscatter profiles of high incidence angle SAR images. *Int. J. Disaster Risk Sci.* **2012**, *3*, 113–122.
17. Marti-Cardona, B.; Dolz-Ripolles, J.; Lopez-Martinez, C. Wetland inundation monitoring by the synergistic use of ENVISAT/ASAR imagery and ancillary spatial data. *Remote Sens. Environ.* **2013**, *139*, 171–184.
18. Martinis, S.; Kersten, J.; Twele, A. A fully automated TerraSAR-X based flood service. *ISPRS J. Photogramm. Remote Sens.* **2015**, *104*, 203–212.
19. Long, S.; Fatoyinbo, T.E.; Policelli, F. Flood extent mapping for Namibia using change detection and thresholding with SAR. *Environ. Res. Lett.* **2014**, *9*, 035002.
20. Clement, M.A.; Kilsby, C.G.; Moore, P. Multi-temporal synthetic aperture radar flood mapping using change detection. *J. Flood Risk Manag.* **2018**, *11*, 152–168.
21. Chini, M.; Pelich, R.; Pulvirenti, L.; Pierdicca, N.; Hostache, R.; Matgen, P. Sentinel-1 InSAR coherence to detect floodwater in urban areas: Houston and hurricane harvey as a test case. *Remote Sens.* **2019**, *11*, 107.
22. Pierdicca, N.; Chini, M.; Pulvirenti, L.; Macina, F. Integrating physical and topographic information into a fuzzy scheme to map flooded area by SAR. *Sensors* **2008**, *8*, 4151.
23. Twele, A.; Cao, W.; Plank, S.; Martinis, S. Sentinel-1-based flood mapping: A fully automated processing chain. *Int. J. Remote Sens.* **2016**, *37*, 2990–3004.
24. Grimaldi, S.; Xu, J.; Li, Y.; Pauwels, V.R.N.; Walker, J.P. Flood mapping under vegetation using single SAR acquisitions. *Remote Sens. Environ.* **2020**, *237*, 111582.
25. Tsyganskaya, V.; Martinis, S.; Marzahn, P. Flood monitoring in vegetated areas using multitemporal Sentinel-1 data: Impact of time series features. *Water* **2019**, *11*, 1938.

26. Henderson, F.M.; Lewis, A.J. Radar detection of wetland ecosystems: A review. *Int. J. Remote Sens.* **2008**, *29*, 5809–5835.
27. Hess, L.L.; Melack, J.M.; Simonett, D.S. Radar detection of flooding beneath the forest canopy: A review. *Int. J. Remote Sens.* **1990**, *11*, 1313–1325.
28. Richards, J.A.; Sun, G.Q.; Simonett, D.S. L-Band Radar Backscatter Modeling of Forest Stands. *IEEE Trans. Geosci. Remote Sens.* **1987**, *GE-25*, 487–498.
29. Cohen, J.; Riihimäki, H.; Pulliainen, J.; Lemmetyinen, J.; Heilimo, J. Implications of boreal forest stand characteristics for X-band SAR flood mapping accuracy. *Remote Sens. Environ.* **2016**, *186*, 47–63.
30. Voormansik, K.; Praks, J.; Antropov, O.; Jagomagi, J.; Zalite, K. Flood mapping with terraSAR-X in forested regions in estonia. *IEEE J. Sel. Top. Appl. Earth Obs. Remote Sens.* **2014**, *7*, 562–577.
31. Pierdicca, N.; Pulvirenti, L.; Chini, M.; Guerriero, L.; Candela, L. Observing floods from space: Experience gained from COSMO-SkyMed observations. *Acta Astronaut.* **2013**, *84*, 122–133.
32. Townsend, P.A. Relationships between forest structure and the detection of flood inundation in forested wetlands using C-band SAR. *Int. J. Remote Sens.* **2002**, *23*, 443–460.
33. Brisco, B.; Schmitt, A.; Murnaghan, K.; Kaya, S.; Roth, A. SAR polarimetric change detection for flooded vegetation. *Int. J. Digit. Earth* **2011**, *6*, 103–114.
34. European Space Agency. Envisat overview. Online available: <https://earth.esa.int/eogateway/missions/envisat/description>. Accessed 12 December 2020.
35. Farr, T.G.; Rosen, P.A.; Caro, E.; Crippen, R.; Duren, R.; Hensley, S.; Kobrick, M.; Paller, M.; Rodriguez, E.; Roth, L.; Seal, D.; Shaffer, S.; Shimada, J.; Umland, J.; Werner, M.; Oskin, M.; Burbank, D.; Alsdorf, D.E. The shuttle radar topography mission. *Rev. Geophys* **2007**, *45*(2), RG2004. <https://doi.org/10.1029/2005RG000183>.
36. Gorelick, N.; Hancher, M.; Dixon, M.; Ilyushchenko, S.; Thau, D.; Moore, R. Google earth engine: planetary-scale geospatial analysis for everyone. *Remote Sens. Environ.* **2017**, *202*, 18–27. <https://doi.org/10.1016/j.rse.2017.06.031>.
37. Hirabayashi, Y.; Mahendran, R.; Koirala, S.; Konoshima, L.; Yamazaki, D.; Watanabe, S.; Kanae, S. Global flood risk under climate change. *Nat. Clim. Change* **2018**, *3*(9), 816–821. <https://doi.org/10.1038/nclimate1911>.
38. Jones, B.; Lamb, R.M. Hazards data distribution system (HDDS) (No. 2015–3048). US Geological Survey, 2015. <https://doi.org/10.3133/fs20153048>.
39. Kawasaki, A.; Berman, M.L.; Guan, W. The growing role of web-based geospatial technology in disaster response and support. *Disasters* **2013**, *37*(2), 201–221. <https://doi.org/10.1111/j.1467-7717.2012.01302.x>.
40. Klein, T.; Nilsson, M.; Persson, A.; Håkansson, B. From open data to open analyses—New opportunities for environmental applications? *Environments* **2017**, *4*(2), 32. <https://doi.org/10.3390/environments4020032>.
41. Kumar, A.; Pandey, A.C.; Khan, M.L. Urban risk and resilience to climate change and natural hazards: a perspective from Million-Plus Cities on the Indian Subcontinent. *Tech. Disaster Risk Manage. Mitigation* **2020**, 33–46. <https://doi.org/10.1002/9781119359203.ch3>.
42. Lal, P.; Prakash, A.; Kumar, A. Google Earth Engine for concurrent flood monitoring in the lower basin of Indo-Gangetic-Brahmaputra plains. *Nat. Hazards* **2020**, *104*(2), 1947–1952. <https://doi.org/10.1007/s11069-020-04233-z>.